Quantifying the Potential of AQPI Gap-Filling Radar Network for Streamflow Simulation through a WRF-Hydro Experiment

YINGZHAO MA,[a,b] V. CHANDRASEKAR,[a] HAONAN CHEN,[a] AND ROBERT CIFELLI[b]

[a] *Colorado State University, Fort Collins, Colorado*
[b] *NOAA/Physical Sciences Laboratory, Boulder, Colorado*

(Manuscript received 22 May 2020, in final form 21 April 2021)

ABSTRACT: It remains a challenge to provide accurate and timely flood warnings in many parts of the western United States. As part of the Advanced Quantitative Precipitation Information (AQPI) project, this study explores the potential of using the AQPI gap-filling radar network for streamflow simulation of selected storm events in the San Francisco Bay Area under a WRF-Hydro modeling system. Two types of watersheds including natural and human-affected among the most flood-prone region of the Bay Area are investigated. Based on the high-resolution AQPI X-band radar rainfall estimates, three basic routing configurations, including Grid, Reach, and National Water Model (NWM), are used to quantify the impact of different model physics options on the simulated streamflow. It is found that the NWM performs better in terms of reproducing streamflow volumes and hydrograph shapes than the other routing configurations when reservoirs exist in the watershed. Additionally, the AQPI X-band radar rainfall estimates (without gauge correction) provide reasonable streamflow simulations, and they show better performance in reproducing the hydrograph peaks compared with the gauge-corrected rainfall estimates based on the operational S-band Next Generation Weather Radar network. Also, a sensitivity test reveals that surficial conditions have a significant influence on the streamflow simulation during the storm: the discharge increases to a higher level as the infiltration factor (REFKDT) decreases, and its peak goes down and lags as surface roughness coefficient (Mann) increases. The time delay analysis of precipitation input on the streamflow at the two outfalls of the surveyed watersheds further demonstrates the link between AQPI gap-filling radar observations and streamflow changes in this urban region.

KEYWORDS: North America; Hydrometeorology; Radars/Radar observations; Hydrologic models

1. Introduction

It is still a challenge to provide accurate and timely flood warning in many parts of the western United States, partially due to the difficulty of having accurate estimates of heavy precipitation and associated timely reliable streamflow predictions (Chen et al. 2020; White et al. 2019; Ralph et al. 2016). To improve monitoring and forecasting of precipitation, streamflow, and coastal flooding in the western United States, especially the San Francisco Bay Area (hereafter referred to Bay Area) of Northern California, the Advanced Quantitative Precipitation Information (AQPI) project is being implemented. The backbone of AQPI is a gap-filling radar network consisting of four X-band radar units and a coastal C-band radar to augment the existing Next Generation Weather Radar (NEXRAD) network, which provides accurate, short-term near surface radar quantitative precipitation estimation (QPE) in the Bay Area.

The radar observation of rainfall and its use in the field of hydrology is an area of ongoing research (e.g., Krajewski and Smith 2002; Seo et al. 2015; Ma and Chandrasekar 2020). It is known that weather radar has an advantage of providing high-resolution observations of precipitation (Bringi and Chandrasekar 2001). Additionally, radar supplies an important source of information for data assimilation in numerical weather prediction models (Gustafsson et al. 2018), which is required for the forecasters to inform storm warning system for flash flood protection. However, radar data have not been widely used in hydrology partially because the accuracy of radar QPE is possibly affected by retrieval errors. In addition, they have different error structures compared with gauge observations and might incorporate associated uncertainties into the hydrological model parameters through calibration (Berne and Krajewski 2013). It is noted that traditional networks of rain gauges often fail to resolve heavy rains and resulting flash flooding at the required spatial and temporal scales but the strength of weather radar information to address this concern is promising (Seo et al. 2015). With the advantage of lower cost, lower power, and easier manipulation, the polarimetric X-band radar system is gaining more interest in urban weather disaster detection (Chandrasekar et al. 2018), and initial assessment showed that the AQPI gap-filling X-band radar has better performance than the S-band NEXRAD in terms of producing higher-quality, higher-resolution QPE in the Bay Area (Cifelli et al. 2018). However, to date it remains unknown

Corresponding author: Y. Ma, yingzhao.ma@colostate.edu

DOI: 10.1175/JHM-D-20-0122.1

about the potential of using the AQPI gap-filling radar network for hydrological forecasting in this urban environment.

The WRF-Hydro modeling framework, which couples the Weather Research and Forecasting (WRF) Model with a hydrological model, offers significant potential for combining hydrological and atmospheric processes in a physically consistent manner (Gochis et al. 2018). Currently, the skill of WRF-Hydro has been tested in various regions all over the world (e.g., Senatore et al. 2015; Yucel et al. 2015; Arnault et al. 2016, 2018, 2019; Naabil et al. 2017; Wehbe et al. 2019; Zhang et al. 2020; Chao et al. 2020; Viterbo et al. 2020). For example, Yucel et al. (2015) evaluated the ability of WRF-Hydro in flood prediction with the WRF-derived precipitation before and after data assimilation. Naabil et al. (2017) explored the potential of WRF-Hydro on water resources planning in the Tono Dam of West Africa. Wehbe et al. (2019) addressed the potential of WRF-Hydro in the short-term hydrological and meteorological predictions in an extreme weather event in an arid region of the United Arab Emirates. Furthermore, Lin et al. (2018) implemented a vector-based river network into the WRF-Hydro to enhance the flood discharge simulation in a hurricane storm event. Arnault et al. (2019) developed a joint soil–vegetation–atmospheric water tagging procedure with WRF-Hydro to assess the contribution of lateral terrestrial water flow on regionally hydrological cycle. Coupled with the height above nearest drainage (HAND) technique, the National Water Model (NWM) system with its core component as WRF-Hydro offers an operational framework for real-time and forecast flood guidance across the contiguous United States (Johnson et al. 2019). As noted above, the WRF-Hydro system has been implemented for a wide range of research and operational prediction problems over the world. However, questions remain regarding catchment response to variability in precipitation intensity and how various hydrologic processes occur under different combinations of land surface–atmosphere conditions remains an active area of research. Also, there are three routing configurations included in the WRF-Hydro system, i.e., Grid, Reach, and NWM, where different configurations can affect the accuracy of model solution and associated streamflow and flood prediction (Gochis et al. 2018). However, there are few studies to address the skill differences of three routing configurations in hydrologic modeling (e.g., Yucel et al. 2015; Naabil et al. 2017; Arnault et al. 2018; Wehbe et al. 2019; Zhang et al. 2020).

The present study aims to quantify the potential of using the AQPI gap-filling X-band radar network for streamflow simulation under the WRF-Hydro modeling framework in the Bay Area, where urban flooding is frequent and results in large impacts to the local economy (Johnson et al. 2020). More specifically, two different watersheds (i.e., natural and human-affected) are selected to address how different catchments respond to various intensity of rainfall in the streamflow simulations. In addition, three routing configurations are intercompared in the two watersheds to clarify their ability in hydrological modeling. Sensitivity analysis with various surficial conditions is also conducted. Meanwhile, the linkage between heavy rainfalls to changes in streamflow is analyzed based on the time delay analysis.

The remainder of this paper is organized as follows: section 2 presents details of WRF-Hydro, including general model description, and three basic routing schemes. Section 3 demonstrates the model experiment for two rainstorm events in the Bay Area. Study area and the WRF-Hydro configurations are also included. Results and discussions are presented in section 4. The main findings are concluded in section 5.

2. The WRF-Hydro modeling framework

a. Model description

The WRF-Hydro modeling system is developed to integrate atmospheric and hydrologic procedures as well as other Earth system processes in a physically consistent manner (Gochis et al. 2018). The version used in this study is 5.0.3, which includes numerous options for terrestrially hydrological routing physics with respect to surface, subsurface, baseflow and channel water movement as well as a lake/reservoir routing scheme. Also, a switch activated module is designed to activate or close the desired modules.

The WRF-Hydro is capable of simulating water and energy fluxes at high spatial and temporal resolutions using a variety of physical and conceptual approaches. Thus, a land surface model (LSM) in both offline and fully coupled modes is developed, where two selections are available, i.e., Noah and Noah-MP (Ek et al. 2003; Niu et al. 2011). The Noah-MP is the updated version of Noah, which has multiple options for LSM parameterizations and simulations. The operation of LSM requires several meteorological forcing variables, including surface precipitation rate, incoming shortwave and longwave radiations, air temperature, specific humidity, surface air pressure, and wind speeds in both horizontal and vertical directions. Using these forcing inputs, the LSM simulates runoff production (e.g., soil infiltration, surface and subsurface overflow, and channel inflow), soil moisture and temperature, canopy energy exchange, and soil moisture versus groundwater interaction, etc. (Niu et al. 2011). In addition, the geographic information system (GIS) tool is implemented with a high-resolution digital elevation model (DEM) to delineate the watersheds and outfalls, stream channel network, lakes/reservoirs, as well as groundwater catchments so as to predict the water fluxes in the domain of interest.

Briefly, the WRF-Hydro is organized in a modularized, FORTRAN 90 style and enables execution on high-performance, parallel computing devices. The operational process begins with initialization of static land surface forcing data, followed by the execution of the gridded LSM, and then activates into terrain routing processes, such as the subsurface, surface, conceptual base flow, and channel and lake/reservoir routings, and finally exports model output and restart files. The disaggregation/aggregation module is also activated for land surface states and fluxes between low-resolution LSM grids and high-resolution terrain routing grids. For more details of WRF-Hydro, the readers are referred to Gochis et al. (2018).

In the WRF-Hydro, there are three basic routing configurations: a gridded routing using diffusive wave method (i.e., Grid), a reach-based routing using the Muskingum–Cunge

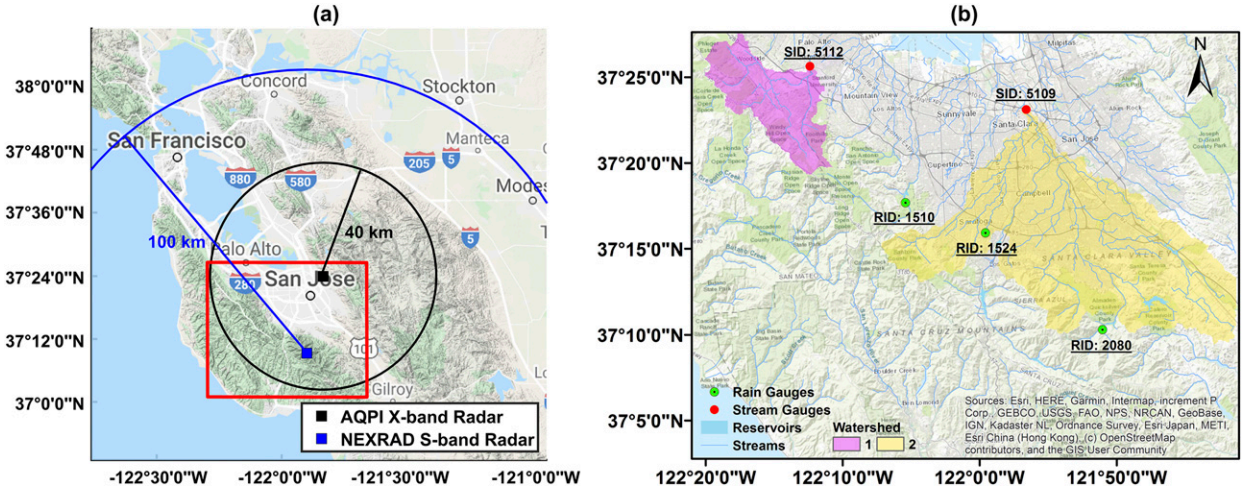

FIG. 1. (a) Locations of AQPI X-band radar and NEXRAD S-band radar in the Bay Area with coverage ranges of 40 km (black) and 100 km (blue), respectively. The red rectangle shows the domain of interest and (b) the study region including two drainage watersheds with two stream gauges (i.e., SIDs 5112 and 5109) and three rain gauges (i.e., RIDs 1510, 1524, and 2080).

(MC) method (i.e., Reach) and the compound National Water Model (i.e., NWM).

b. Grid

In the grid-based routing configuration, a diffusive wave formulation with one-dimensional (1D), variable time-stepping is applied in the pixel-by-pixel grid channel network. It is based on the general St. Venant equation for shallow water flow movement (Garcia and Kahawita 1986). Given deeper flow in the channel, a dynamic propagation with variable time-stepping can resolve highly variable flood waves. Usage of variable time-stepping may induce potential computation problems, and it is thus recommended to set up an appropriate time-scale factor for this model execution. Moreover, both the lake/reservoir and conceptual base flow modules are activated.

c. Reach

In the reach-based routing configuration, the 1D vectored channel network is built from the gridded catchment and

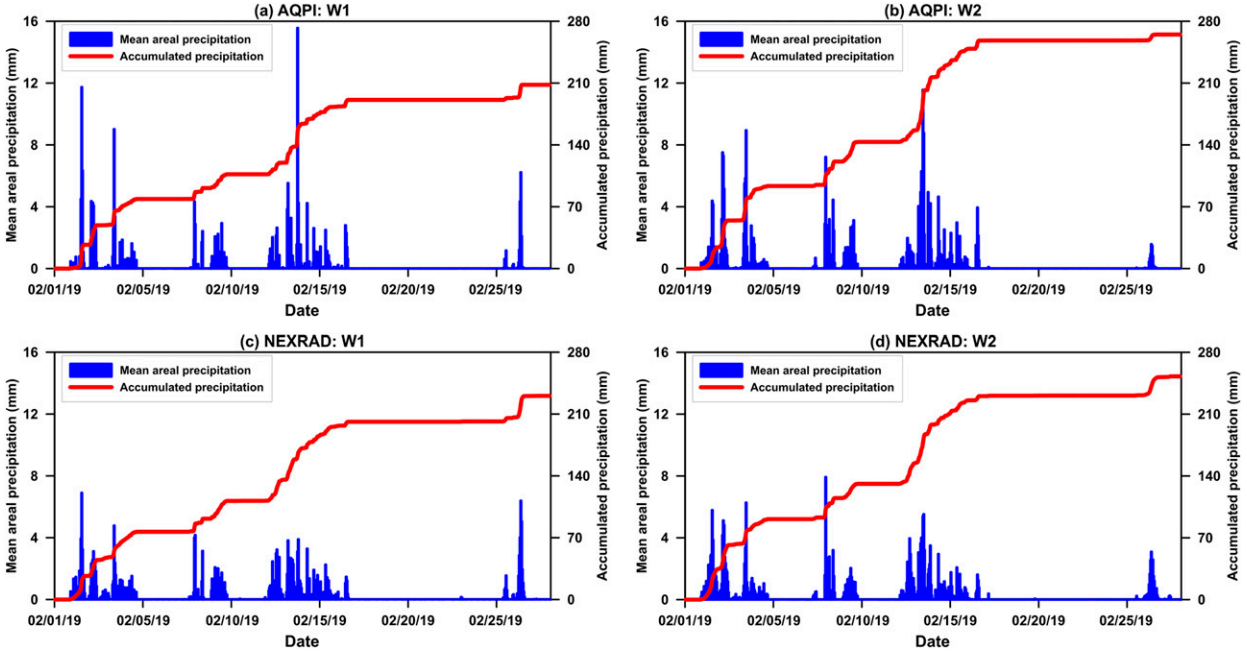

FIG. 2. The hourly mean areal precipitation and its accumulation in February 2019 in the two watersheds from (a),(c) the AQPI data and (b),(d) the NEXRAD data.

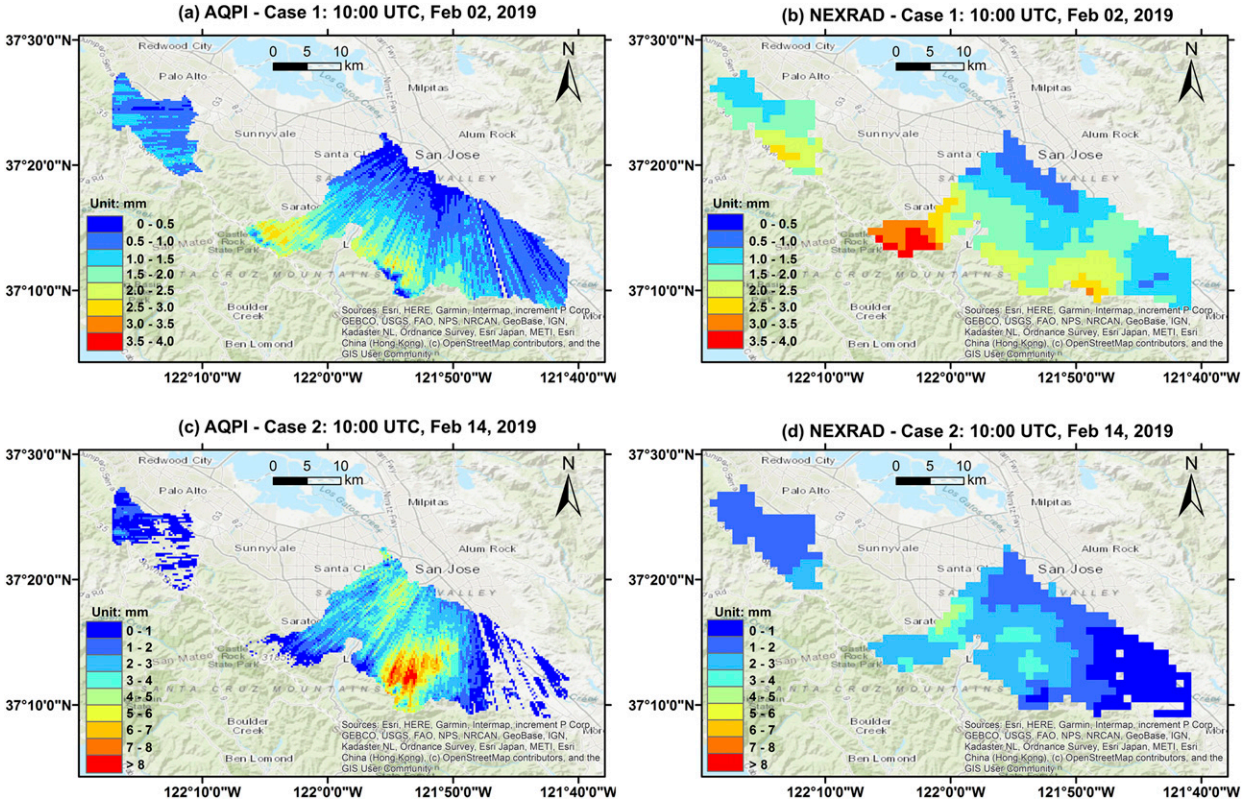

FIG. 3. The spatial distribution of hourly rainfall in the two watersheds from both AQPI and NEXRAD data for (a),(b) 1000 UTC 2 Feb and (c),(d) 1000 UTC 14 Feb 2019.

drainage network. The routing flow moves water from upstream to downstream and accumulates at the channel junctions through the linked stream network. In the river flow simulation, a MC method is implemented for calculating the hydrograph routings. A conceptual base flow module is activated. However, the option to activate/inactivate the lake/reservoir module is not developed in the reach-based scheme unless the user is running the NWM configuration.

d. NWM

The NWM is implemented under the WRF-Hydro modeling system, but some physics options differ from the grid-/reach-based routing configurations. After the LSM loop, the disaggregation/aggregation routine is performed as an independent operation, which needs a user-defined mapping file (i.e., "spatialweights.nc"). It is used to translate from the gridded fluxes and states to aggregated catchment fluxes and states, and then pass into the reach-based routing for river flow calculation. The spatialweights.nc file contains spatial weights and identification of all polygons from one input shapefile that intersects each polygon in another input shapefile. Also, it supports the calculation of contributed proportion of each grid on the channel flow fluxes.

In the NWM, the surface overland and subsurface flow routings are calculated based on a steepest descent method, and the channel routing is simulated using a MC approach with a fine spatial resolution. The surface and subsurface flow routings are the same with the grid-based scheme, and the channel flow routing is the same with the reach-based scheme. The lake/reservoir module is activated like the grid-based routing configuration. Additionally, a conceptual base flow module is activated like the grid-/reach-based routing configurations, but the groundwater basin file and bucket parameters are utilized based on the user-defined mapping file.

3. An experiment on February 2019 rainstorms in the Bay Area

a. Study area and dataset

The experiment was performed in the Bay Area during the atmospheric river (AR)-driven storms that occurred in February 2019. The Bay Area is the second largest urban region in California and is one of the fastest growing economies in the United States. Figure 1a shows the geographic locations of an AQPI X-band radar and a NEXRAD S-band radar in the Bay Area. The coverage ranges of the AQPI and NEXRAD radars are 40 and 100 km, respectively. To quantify the value of AQPI radar on streamflow simulation, the WRF-Hydro domain is setup in Fig. 1b, where two types of watersheds are investigated. Watershed 1 (W1) is natural with no lakes/reservoirs and its area is 91.7 km^2. Watershed 2 (W2) is human-affected with some reservoirs and its area is 4.5 times of W1. In the domain, the 20-category MODIS land cover data, derived from the WRF preprocessing tool (WPS) version 4.0, is

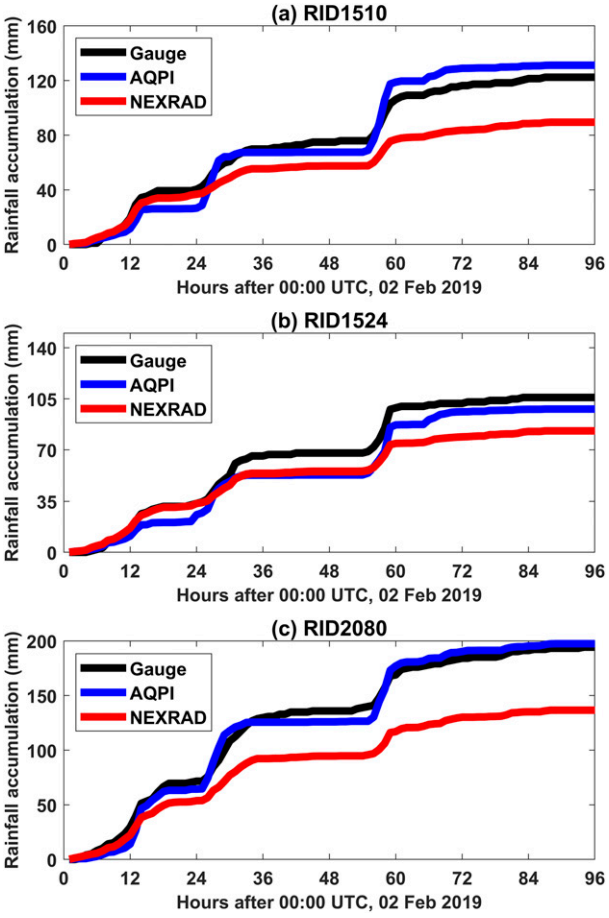

FIG. 4. Intercomparison of hourly rainfall accumulation for Case 1 with the AQPI, NEXRAD, and ground references (Gauge) data at the grid location of RIDs (a) 1510, (b) 1524, and (c) 2080, respectively.

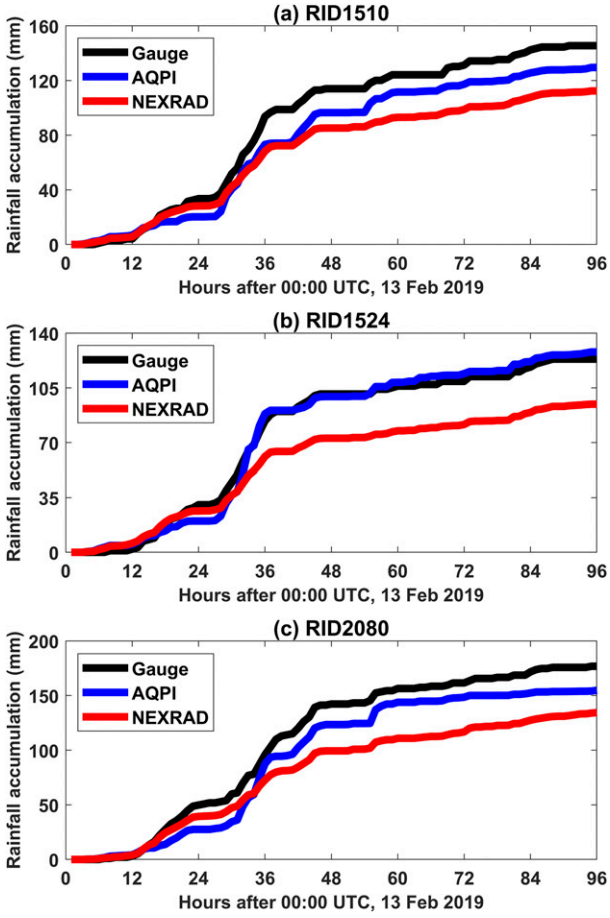

FIG. 5. As in Fig. 4, except for Case 2.

used in this study. The stream gauges deployed at the outfalls of W1 and W2 (i.e., SIDs 5112 and 5109, respectively) are used for evaluating the modeled streamflow. In addition to the near-real-time (i.e., 2 min) AQPI radar QPE with a spatial resolution of 250 m × 250 m as the specific precipitation forcing, the gauge-corrected hourly NEXRAD rainfall product (hereafter referred to as NEXRAD) with a spatial resolution of 1 km × 1 km, which is produced by the operational Multi-Radar Multi-Sensor system (Zhang et al. 2011), is also incorporated in this analysis. However, for fair comparison with NEXRAD, analysis of the AQPI product is performed at hourly scale. Three rain gauges (i.e., RIDs 1510, 1524, and 2080) are used for cross examining the two radar rainfall estimates in the AR storm events.

Figure 2 shows the time series of the mean areal precipitation (MAP) in the two watersheds from both the AQPI and NEXRAD data in February 2019. There are two major storms, including 2–5 February (Case 1) and 13–16 February (Case 2). With respect to the AQPI data, the accumulated MAP in W1 (W2) is 78.3 (92.8) mm for Case 1, and 76.5 (105.4) mm for Case 2, respectively. In terms of the NEXRAD data, the corresponding accumulated MAP in W1 (W2) are 75.9 (90.4) mm for Case 1, and 84.4 (94.5) mm for Case 2, respectively. The two events are part of a series of storms in 2019 that produced over $100 million in flood-related damages (Johnson et al. 2020), and the impacts from the AR storm centered on 14 February 2019 include riverine and alluvial flash flooding, landslides, and disruptions to transportation, etc. (Hatchett et al. 2020). In addition, there are two moderate rainfall events: one is during 8–10 February 2019 and the other is during 26–28 February2019. The accumulated MAP from the AQPI data in W1 (W2) are 28 (50) mm and 17.1 (6.8) mm, respectively, for the two moderate rainfall cases.

The land surface data in the domain are obtained from WPS, which archives a database of land cover type, soil, and vegetation initial conditions across the globe. The DEM data used for creating hydrologic routing files are at 90 m × 90 m resolution, which are derived from the Shuttle Radar Topographic Mission (SRTM). As for the atmospheric forcing data, the North American Land Data Assimilation System Project Phase 2 (NLDAS-2) with a 1/8° grid and hourly time step are used (Xia et al. 2012). As for NLDAS-2 data, the height information of surface pressure, radiation and precipitation is at the surface, the height information of air temperature and specific humidity is at 2 m above the surface, and the height information of wind field is at 10 m above the surface.

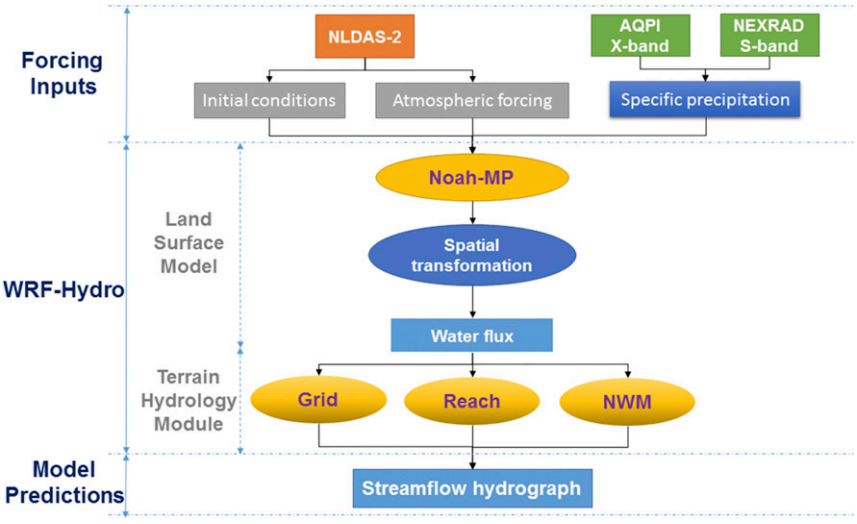

FIG. 6. The flowchart of WRF-Hydro modeling system used in this study.

b. *Statistical error metrics*

To illustrate the performance of streamflow simulations for the rainstorm events, three error metrics are used, including normalized mean absolute error (NMAE), root-mean-square error (RMSE), and Kling–Gupta efficiency (KGE). Their formulas are given below:

$$\mathrm{NMAE} = \frac{\langle|\mathrm{Sim} - \mathrm{Obs}|\rangle}{\langle\mathrm{Obs}\rangle} \times 100\%, \tag{1}$$

$$\mathrm{RMSE} = \sqrt{\langle(\mathrm{Sim} - \mathrm{Obs})^2\rangle}, \tag{2}$$

$$\mathrm{KGE} = 1 - \sqrt{\langle(r-1)^2\rangle + \langle(\alpha-1)^2\rangle + \langle(\beta-1)^2\rangle}, \tag{3}$$

where Sim and Obs are the simulated and observed data for the event durations, respectively; the angle brackets stand for sample average; r is the Pearson's correlation coefficient between simulation and observation; α is a measure of relative variability in the simulated and observed data; and β is the bias of the simulated values, i.e., the ratio between the mean simulated and mean observed data. The KGE value ranges from $-\infty$ to 1 with 1 as the best skill score. Given that KGE can identify possible sources of errors from mean, variance, and correlation components from the ideal point (Gupta et al. 2009), the KGE index is selected instead of the Nash–Sutcliffe efficiency for the measure of model performance.

c. *AQPI gap-filling radar rainfall analysis*

Figure 3 presents the spatial distribution of hourly rainfall during the two storms at 1000 UTC 2 February 2019 and 1000 UTC 14 February 2019, respectively, using both the AQPI and NEXRAD products. The AQPI data provide more details of precipitation structure in the two watersheds due to its higher spatial resolution (250 m × 250 m) compared with the lower resolution of NEXRAD data (1 km × 1 km). Also, some bias exists between the two products due to various rainfall retrieval algorithms used by the AQPI and NEXRAD radar systems. The AQPI radar rainfall is derived from the R–K_{dp} (R, rainfall; K_{dp}, specific differential propagation phase), whereas the NEXRAD product is based on Z–R relation (Z, reflectivity) and is further adjusted by gauge data (Cifelli et al. 2018; Zhang et al. 2011). To verify the rainfall performances of AQPI and NEXRAD, the two products are intercompared with the ground references (Gauge) at three gridcell sites (i.e., RIDs 1510, 1524, and 2030) in the Bay Area in the two rainstorm events of February 2019. Visual inspections of Fig. 4 (Case 1) and Fig. 5 (Case 2) illustrate that the AQPI X-band radar agrees better with gauge estimates compared to NEXRAD at all the grid locations and can provide reasonable QPE without gauge-based correction. More details of the AQPI radar rainfall analysis in the Bay Area can be found in Cifelli et al. (2018).

d. *WRF-Hydro model configuration*

The flowchart of WRF-Hydro used in this paper is shown in Fig. 6, where an offline mode is configured in this application. The Noah-MP option is applied for vertical land surface parameterization. The option for dynamic vegetation in the vegetation model is turned off for simplicity. The Ball–Berry (BB) model is used to simulate canopy stomatal resistance. The original surface and subsurface runoff, i.e., free drainage, is set for runoff and groundwater option. The Monin–Obukhov (MO) scheme is applied to calculate the surface layer drag coefficient. The option for supercooled liquid water or ice fraction is assumed as no iteration. The linear effect and more permeable option is adopted for frozen soil permeability. The two-stream scheme that applies to vegetated fraction is selected for the radiation transfer process. As for the ground snow surface albedo, it is calculated from the Canadian Land Surface Scheme (CLASS) model. The partitioning of precipitation into rainfall and snowfall is based on the method of Jordan (1991). The surface resistance to evaporation/sublimation is retrieved from Sellers et al. (1992). Details of optional parameterizations can be found in Yang et al. (2011).

The Noah-MP LSM module, which is capable of simulating land–atmosphere interaction processes using multiple options (Niu et al. 2011), is run with the grid cell at 1 km × 1 km resolution and used the NLDAS-2 as the atmospheric forcing inputs except for precipitation rate. Both the AQPI and NEXRAD rainfall products are used as the specific precipitation forcing to compare the difference of streamflow responses. The NLDAS-2 forcing and optional radar rainfall inputs are resampled into a 1 km × 1 km grid resolution using the WRF-Hydro regridding script.

For each hourly time scale at which the atmospheric forcing data are available, the column moisture flux within the Noah-MP is disaggregated from the LSM grid (1 km × 1 km) to the routing grid at 100 m × 100 m using a subgrid disaggregation–aggregation transformation method and transferred to the terrain and channel routing processes. The time steps for the terrain and channel routing processes are 10 and 100 s, respectively. The aggregation factor 10 is used to ensure the overland/subsurface flow processes, and the grid disaggregation approach results in 100 cells in total at 100 m × 100 m resolution for each LSM grid.

The WRF-Hydro initialization file is created by the ''create_WRFinput.R'' script from a WPS GEOGRID file and a set of user-specified conditions. It includes the initial conditions (e.g., initial model states of soil moisture, soil temperature, skin temperature, etc.) for a cold start of the WRF-Hydro system. The WRF-Hydro is ''cold'' started from 0100 UTC 1 January to 0000 UTC 1 February 2019 to ensure the state variables reach equilibrium in the spinup period. Based on the restart files at 0000 UTC 1 February 2019, the model is ''warm'' started and calibrated on Case 1. During the spinup and calibration periods, the WRF-Hydro is implemented with NLDAS-2 as meteorological forcing and the AQPI rainfall product as specific precipitation under the NWM routing configuration. Several key parameters related to soil, runoff, groundwater, and channel modules are selected by the WRF-Hydro Development Team to regionally calibrate NWM Version 1.1 in the contiguous United States (Dugger et al. 2017; Lahmers et al. 2019). In this study, these parameters are selected and calibrated using the dynamically dimensioned search (DDS) algorithm with 250 iterations (Tolson and Shoemaker 2007), and corresponding hydrographs of simulated streamflow at the two outfalls in the calibration period of Case 1 are shown in Fig. 7. The calibrated parameters are utilized based on the optimization of the KGE performance metric at the two outfalls, and the red curves in Figs. 7a and 7b show the optimally simulated streamflow hydrographs in the calibration process, respectively. Table 1 lists the optimal model parameters used in this study.

Based on the calibrated optimal parameters and restart files at 0000 UTC 6 February 2019, the model is ''warm'' started to ensure an additional spinup of a week and validated on Case 2. In the validation period, the potential of the AQPI radar for accurate streamflow simulation through the WRF-Hydro system is investigated with the three routing configurations noted in section 2; also, we compare the AQPI-based streamflow with the NEXRAD-based result under the NWM-based WRF-Hydro system. Moreover, both the sensitivity of surficial conditions on streamflow and the time delay from rainstorm to discharge are analyzed using the AQPI gap-filling radar as the precipitation forcing source and the NWM as the routing configuration in the WRF-Hydro system.

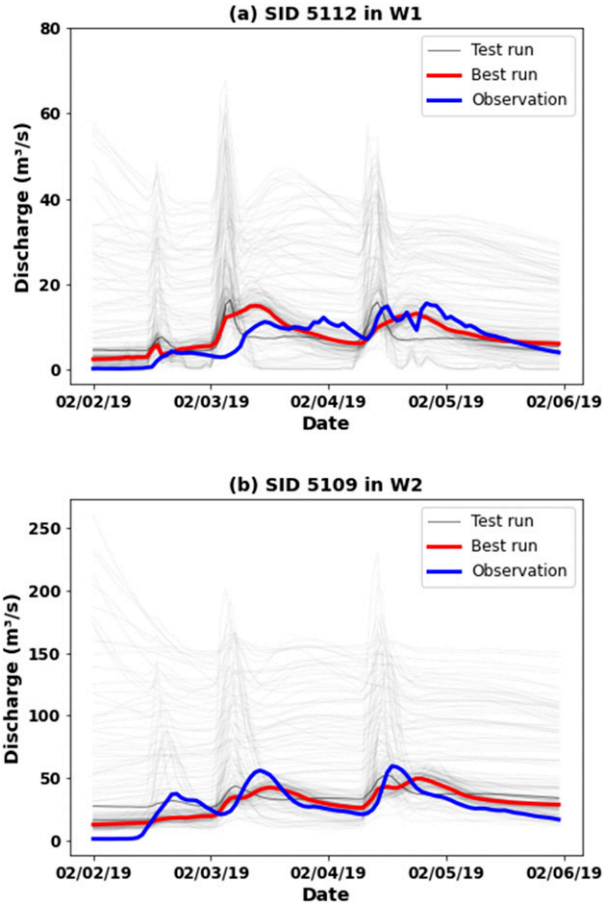

FIG. 7. Changes in streamflow at two outfalls, i.e., SIDs (a) 5112 and (b) 5109, in the two watersheds (i.e., W1 and W2) in the calibration period of 2–5 Feb 2019. In each panel, the gray curves show the test run with 250 iterations and the red curve indicates the best run in the calibrated process; the observed streamflow in each panel is also shown as the blue curve.

4. Results and discussion

a. *Model evaluation of various routing configurations*

Figure 8 illustrates the performance of simulated streamflow at the two outfalls (i.e., SIDs 5112 and 5109) of W1 and W2 in the validation period of Case 2 with the three routing configurations in WRF-Hydro using the AQPI radar QPE as the precipitation forcing.

During the validation period, there is a widespread rainstorm in the Bay Area. The highest hourly MAP in W1 (15.6 mm) occurs between 1700 and 1800 UTC 14 February 2019. Two peaks are observed in the outfall of W1 on 14 February 2019: the first one, 32.1 $m^3 s^{-1}$, occurs at 1600 UTC due to continuous light–moderate rainfall in the past 24 h, and

TABLE 1. The selected optimal model parameters used in the study.

Type	Parameter	Description	Unit	Value or range
Soil	Bexp	Pore size distribution index	Dimensionless	3.62–9.83
	smcmax	Saturation soil moisture content (i.e., porosity)	Volumetric fraction	0.41–0.96
	dksat	Saturated hydraulic conductivity	$m\ s^{-1}$	9.7×10^{-7}–1.4×10^{-5}
Channel	Bw	Parameterized width of the bottom of the stream network	m	0.53
	Mann	Manning's roughness coefficient	Dimensionless	0.029
	ChSlp	Channel side slope	$m\ m^{-1}$	0.018
Runoff	REFKDT	A tuneable parameter that significantly impacts surface infiltration and hence the partitioning of total runoff into surface and subsurface runoff	Unitless	4.95
	slope	Linear scaling of "openness" of bottom drainage boundary	Unitless	0.176
	RETDEPRTFAC	Multiplier on retention depth limit	Unitless	0.257
	LKSATFAC	Multiplier on lateral hydraulic conductivity	Unitless	2732
Groundwater	Zmax	Maximum groundwater bucket depth	mm	174.9
	Expon	Exponent controlling rate of bucket drainage as a function of depth	Dimensionless	3.85

the second one, 35.3 $m^3\ s^{-1}$, occurs at 2200 UTC due to higher-intensity rainfall over the last several hours (Fig. 8a). The NWM at SID 5112 produces a single peak flow of 15.9 $m^3\ s^{-1}$ about 3 h after the hourly MAP peak in W1, which underestimates the magnitude and straddles the timing of the two observed peak flows. As for the Grid configuration, the simulated peak flow occurs at the same time as the second observed peak but the amount is smaller (27 $m^3\ s^{-1}$ versus 35.3 $m^3\ s^{-1}$). For the Reach configuration, the simulated peak flow (34.4 $m^3\ s^{-1}$) is similar in magnitude to both the first and second observed peaks and occurs between 1800 and 1900 UTC, and about 1 h later after the hourly MAP in W1. Also, as shown in Table 2, the Reach scheme has better skills than both Grid and NWM schemes. Overall, it shows that the WRF-Hydro simulated streamflow is sensitive to routing configurations, but the response time of the simulated peak streamflow is faster, and the magnitude of the model simulations is severely underestimated compared with the observed hydrograph pattern. As shown in Fig. 5a, there is an underestimation of AQPI radar QPE compared with gauge observations in W1, which is likely one of the reasons that leads to the underprediction of peak flow in the WRF-Hydro simulations.

In W2, the maximum hourly MAP is 11.6 mm and occurs at 1100 UTC 14 February 2019. The observed peak flow in SID 5109 (125.4 $m^3\ s^{-1}$) comes 4 h after the maximum hourly MAP, which is 1 h earlier in occurrence, but 3 times larger in magnitude, than the first observed peak in SID 5112 of W1. The NWM simulates a peak streamflow of 74.8 $m^3\ s^{-1}$ at 2200 UTC,

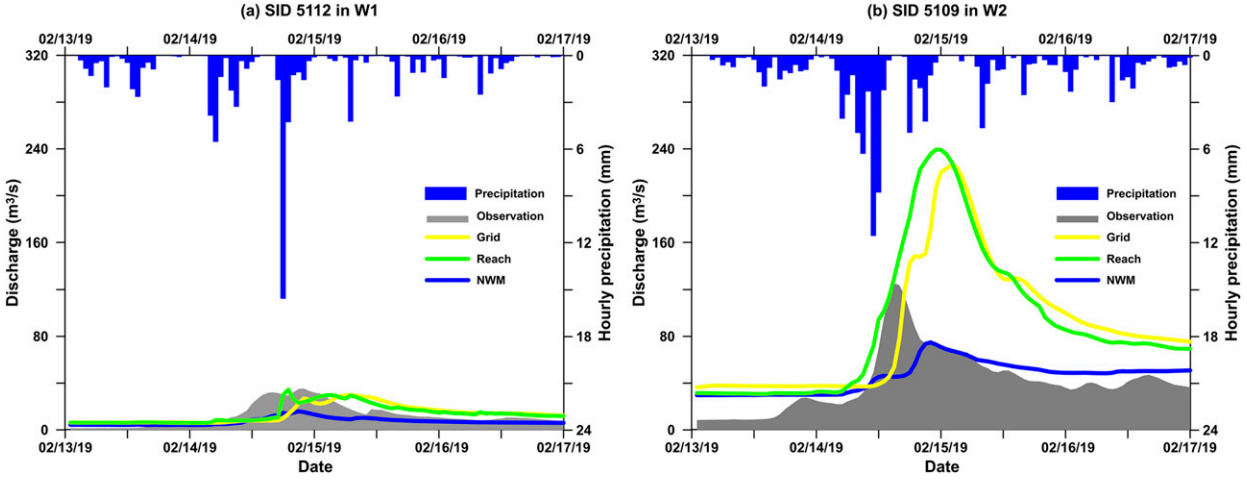

FIG. 8. Simulated and observed hourly streamflow at the two outfalls, i.e., SIDs (a) 5112 and (b) 5109, in the two watersheds (i.e., W1 and W2) in the validation period of 13–16 Feb 2019. The simulated streamflow is separately modeled by the WRF-Hydro system with three routing configurations including Grid (yellow), Reach (green), and NWM (blue) using the AQPI product as precipitation forcing input. In each panel, the observed streamflow is indicated with gray shading, and the hourly mean areal precipitation in each watershed derived from the AQPI radar is displayed as blue bars.

TABLE 2. Statistical error indices (i.e., NMAE, RMSE, and KGE) of simulated streamflow at the two outfalls (i.e., SIDs 5112 and 5109) in the two watersheds (i.e., W1 and W2) in the validation period of 13–16 Feb 2019. The simulations are accomplished by three routing configurations including Grid, Reach, and NWM in the WRF-Hydro system using the AQPI radar product as precipitation forcing input. Also, the simulated streamflow is performed under the NWM-based WRF-Hydro using the NEXRAD product as precipitation forcing input.

Stream gauges	Mode type	NMAE (%)	RMSE ($m^3 s^{-1}$)	KGE
SID 5112, W1	AQPI_Grid	52.9	8.47	0.48
	AQPI_Reach	42.6	7.04	0.63
	AQPI_NWM	49.2	8.49	0.20
	NEXRAD_NWM	46.7	8.50	0.20
SID 5109, W2	AQPI_Grid	124.5	64.57	−0.59
	AQPI_Reach	117.6	66.38	−0.79
	AQPI_NWM	32.8	20.65	0.38
	NEXRAD_NWM	30.0	20.25	0.29

several hours later and with a magnitude about 60% compared to the observed peak. As the rain event continues after the highest rainfall recorded in W2, both the observed and NWM-simulated discharges decrease to a stable level of 40–50 $m^3 s^{-1}$ (Fig. 8b). In contrast to the NWM result, both the Grid and Reach routing simulations significantly overestimate the peak flow in W2, with discharge values of 226.4 and 239.4 $m^3 s^{-1}$, respectively. Also, the timings of these peak flows lag the observed peak at SID 5109 even more than the NWM simulation with the Grid and Reach simulations occurring at 0200 UTC 15 February and 2300 UTC 14 February, respectively. Each hydrograph in the two watersheds shows a streamflow response to the rainfall event, but the Grid and Reach require a longer time to achieve the peak flow than the NWM in W2. As learned from Fig. 9, it is obvious that the Grid/Reach schemes have significant biases in terms of NMAE, RMSE, and KGE at the outfall of W2.

In the natural watershed, W1, with its area less than 100 km^2, the Grid/Reach schemes are more appropriate for modeling the in/outflow processes, and the NWM is not clearly the superior routing configuration for streamflow simulation in the rain event. The primary reason might be due to the deficiency in the disaggregation/aggregation routine configured in the NWM system in this small watershed with less than 100 grid cells and no reservoirs. In the human-affected W2 basin with its drainage area more than 400 km^2, there are substantial overestimations of event volumes for both Grid and Reach routing configurations in the validation period, and the Reach scheme shows a higher overestimation at the flow peak than that of the Grid mode. At least for the mid-February 2019 storm analyzed, the Reach scheme fails to perform well for streamflow simulation. The MC algorithm based on flow hydraulics, channel storage, and lateral inflow contribution is used for the reach-based river network (Gochis et al. 2018). During the storm event, an infiltration excess situation occurs but the MC method does not consider the impact of the backwater effect, which may increase the channel flow in the river network and result in higher runoff volume (Fig. 8b). Also, in the Reach scheme, the option of lake/reservoir process is not activated, which would incur a larger bias for the simulated streamflow. The reason of large magnitude of streamflow produced from the Grid scheme in the hydrograph of SID 5109 is due to excessive water fluxes and states translating from fine grids to the aggregated catchment in W2. Overall, the NWM scheme shows the most satisfying performance for streamflow simulation among the three routing configurations in W2 and indicates

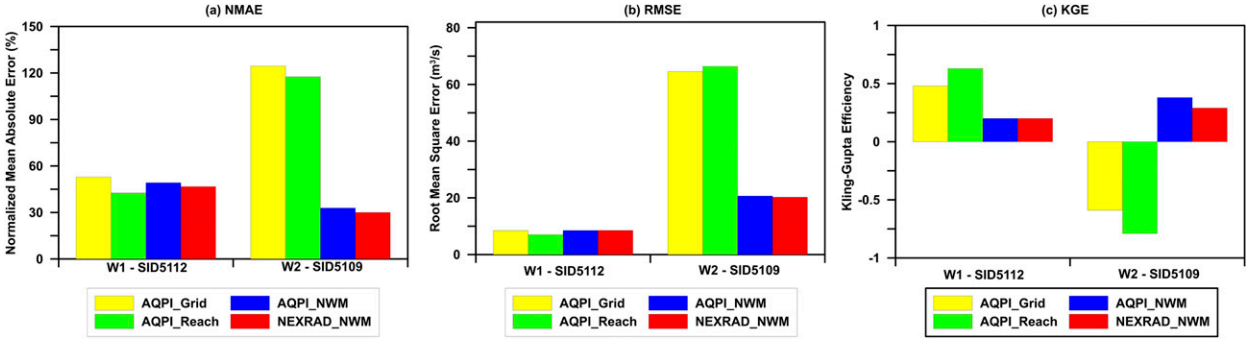

FIG. 9. Statistical error indices (i.e., NMAE, RMSE, and KGE) of simulated streamflow at the two outfalls (i.e., SIDs 5112 and 5109) in the two watersheds (i.e., W1 and W2) in the validation period of 13–16 Feb 2019. The simulations are performed by three terrain routing schemes including Grid (yellow), Reach (green), and NWM (blue) in the WRF-Hydro system using the AQPI product as precipitation forcing input. Also, the simulation is performed in the NWM-based WRF-Hydro system using the NEXRAD product as precipitation forcing input, which is shown as red bar in each panel.

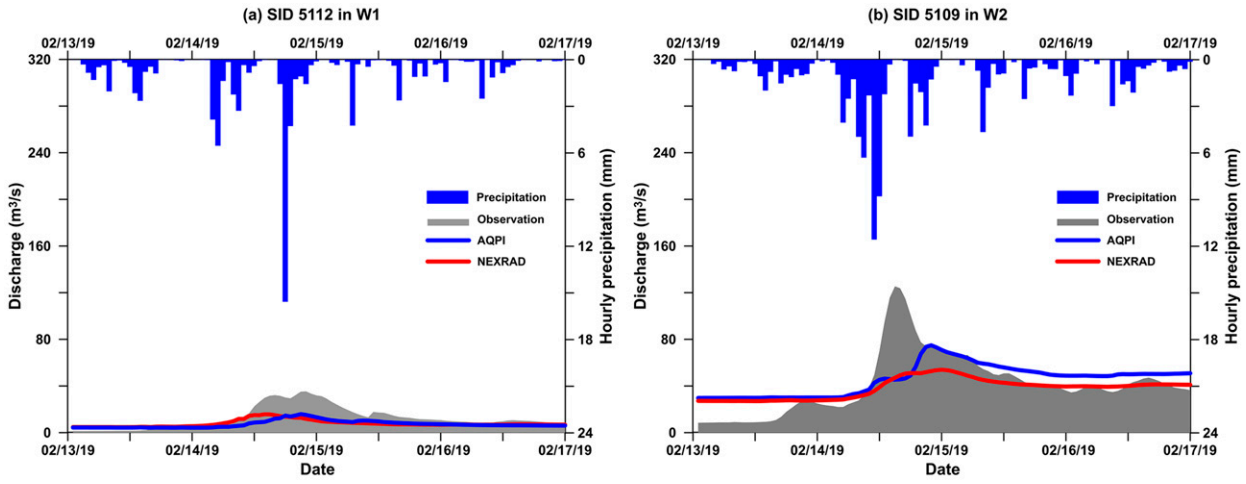

FIG. 10. Simulated and observed hourly streamflow at the two outfalls, i.e., SIDs (a) 5112 and (b) 5109, in the two watersheds (i.e., W1 and W2) in the validation period of 13–16 Feb 2019. The simulated streamflow is separately modeled by the NWM-based WRF-Hydro system using the AQPI (blue) and NEXRAD (red) product as precipitation forcing input. In each panel, the observed streamflow is shown with gray shading, and the hourly mean areal precipitation in each watershed derived from the AQPI radar is displayed as blue bars.

that the consideration of lake/reservoir module is important for obtaining accurate streamflow simulation in the WRF-Hydro system for this managed basin. However, the results also imply that all the schemes are still challenged for producing accurate streamflow simulations in this heavy rain event, e.g., Case 2. More research is necessary on this issue to improve the WRF-Hydro system in events like the storms analyzed herein. It is further noted that the WRF-Hydro system is calibrated with the NWM scheme, which may favor the flow comparisons when comparing three routing configurations.

b. *Model evaluation of various radar rainfall inputs*

Figure 10 presents the performances of simulated streamflow at two outfalls (i.e., SIDs 5112 and 5109) of W1 and W2 in the validation period with two different radar rainfall inputs (i.e., AQPI and NEXRAD) in the NWM-based WRF-Hydro system. This figure shows that neither simulation using the two different precipitation inputs is able to reproduce all the details of the hydrographs in the mid-February 2019 storm event. The NEXRAD exhibits slightly better NMAE scores for the streamflow simulations compared with that of AQPI radar product (Fig. 11c). For W2, the timing of the peak flow is earlier in the NEXRAD-forced simulation and more similar with observations than the AQPI-forced simulation though the magnitude of the NEXRAD-forced simulation is smaller. This may be due to less rainfall observed by NEXRAD as shown in Fig. 5. However, for both watersheds the AQPI rainfall product has an advantage in simulating the streamflow peak compared with NEXRAD. Specifically, the performance of simulated streamflow driven by the AQPI data has higher KGE (0.38) than that forced by NEXRAD (0.29) in W2 in the validation period (Table 2). Taken together, these results demonstrate that the AQPI radar can provide reasonable streamflow simulations without gauge-based correction in the AR-driven rainstorm event. It should be noted that AQPI radar data are used as the rainfall forcing to calibrate the model, and some AQPI-driven error could be compensated by the model parameter set. The resultant streamflow simulations might be more favorable than those forced by the NEXRAD product.

To some extent, the statistics from both AQPI and NEXRAD radar QPE at SID 5109 show the capability of the NWM scheme in streamflow simulation in the human-affected watershed (Table 2). However, as seen from the hydrographs driven by either radar product, both fail to simulate the streamflow peak very well in the validation period. An obvious underestimation is found for the streamflow simulation in the two basins. This is a reminder that there is still room for improving the performance of the NWM-based WRF-Hydro system on flood prediction during this extreme rainstorm event.

c. *Sensitivity analysis on streamflow changes with various surficial conditions*

Streamflow response to extreme rainfall is sensitive to land surface conditions for most hydrological applications (Yucel et al. 2015; Sharma et al. 2018; Rummler et al. 2019). To address this critical issue, a sensitivity test is performed to demonstrate the changes in discharge from various surficial conditions in the NWM-based WRF-Hydro system using the AQPI radar QPE as the precipitation input in the human-affected W2 in the mid-February 2019 storm. Both the overland and channel parameters are explored as these parameters are more sensitive in the streamflow simulation compared to other parameters (e.g., groundwater or LSM) (Yucel et al. 2015; Lahmers et al. 2019). Considering that the infiltration factor (i.e., REFKDT) and Manning's roughness coefficient (i.e., Mann) are two principally sensitive parameters of the WRF-Hydro system that impact the rainfall–runoff response characteristics (Yucel et al. 2015; Liu et al. 2021), REFKDT and Mann are selected in this sensitivity analysis.

Figure 11 shows the performance of simulated streamflow with REFKDT ranging from 1.0 to 5.0 in 1.0 increments and

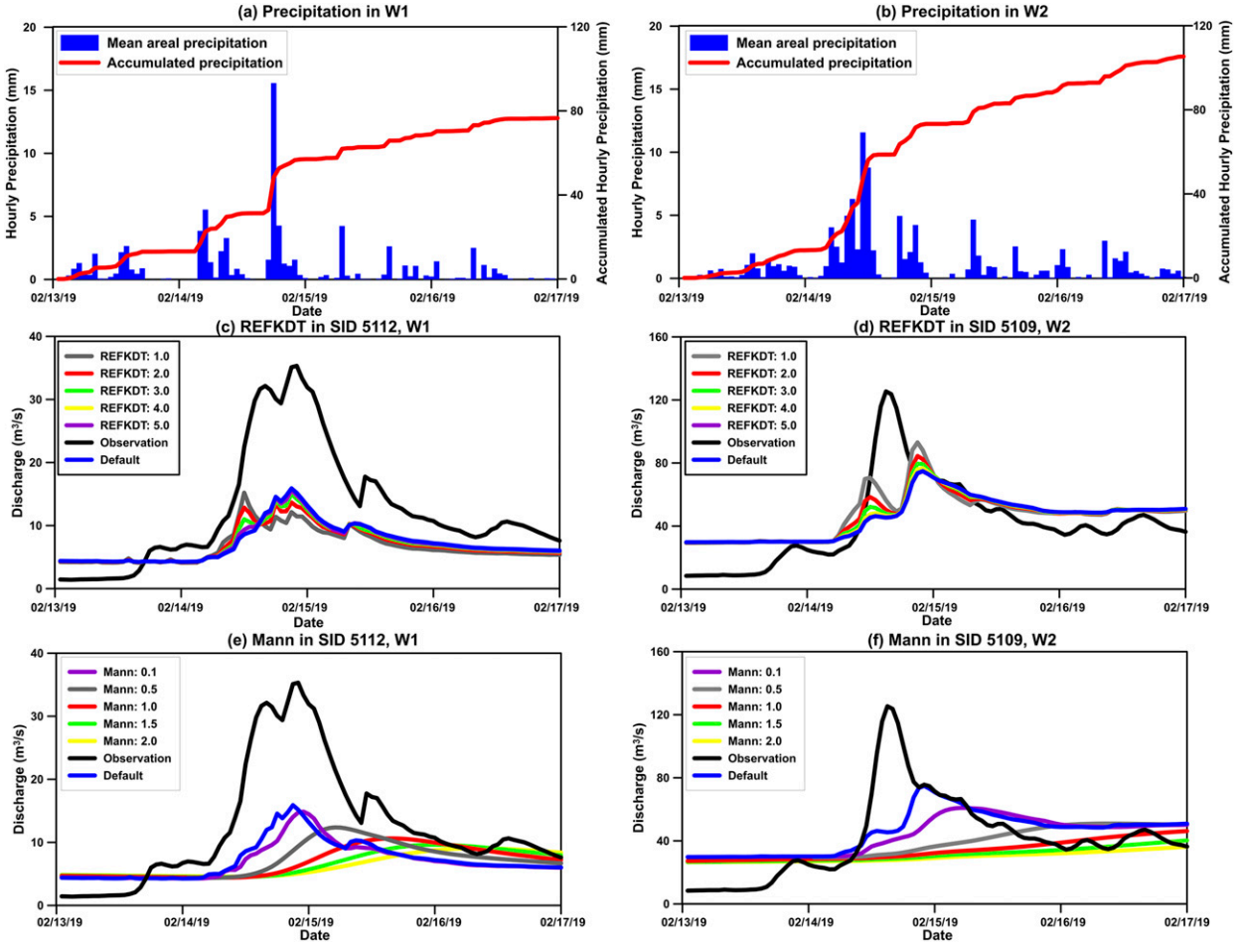

FIG. 11. Sensitivity analysis to explore the streamflow response based on the NWM-based WRF-Hydro system at SIDs 5112 and 5109 of the two watersheds in the mid-February 2019 storm event. (a),(b) The hourly mean areal precipitation and its accumulation in each watershed are shown; the sensitivity analysis of (c),(d) infiltration factor (i.e., REFKDT) and (e),(f) Manning's roughness coefficient (i.e., Mann) at each outfall are also shown. The observed and simulated streamflow using the default values of REFKDT and Mann are shown as black and blue curves, respectively.

Mann ranging from 0.1 to 2.0 with 0.5 increments in the two watersheds. The observed and simulated streamflow using the default values of REFKDT and Mann are also shown as black and blue curves, respectively. All the curves correspond to the observed flow trends and the occurrences of most peaks are well simulated at the two outfalls (i.e., SIDs 5112 and 5109) for both REFKDT and Mann parameters. Additionally, as the rainfall decreases from 0000 UTC 15 February, both the observed and simulated streamflow become lower for each parameter. According to the simulated result of REFKDT at the two outfalls, as REFKDT increases from 1.0 to 5.0, the hydrograph volume declines for the simulated peak, but it gradually increases the volume during the recession portions of the hydrograph. This implies that the simulated hydrograph is very sensitive to REFKDT in the NWM scheme. Considering that REFKDT is a tunable parameter that impacts surface infiltration and hence the partitioning of total runoff into surface and subsurface runoff, the lower value of REFKDT would provide more water flux into the channel flow, especially in the human-influenced W2. Based on the corresponding curves of the Mann parameter in Figs. 11e and 11f, the simulated peak decreases and lags in both watersheds as the surface roughness index increases from 0.1 to 2.0. Because Manning roughness coefficient has an impact on the channel environment, a higher value can hamper the water flow movement and decrease the peak flow. A longer time is thus necessary to accumulate the peak flow and corresponding lags are detected for increasing the Mann parameter in both watersheds. These results shown herein of the two parameters demonstrate the importance of surficial conditions on the streamflow response to rain event.

d. Time delay analysis from rainstorms to streamflow changes

The time response from rainfall occurring in a storm to the resulting discharge is very complex, which varies with watershed size and shape, as well as storm scale and storm velocity (Cristiano et al. 2017). It is well known that the cross-correlation function (CCF) is beneficial for exploring the

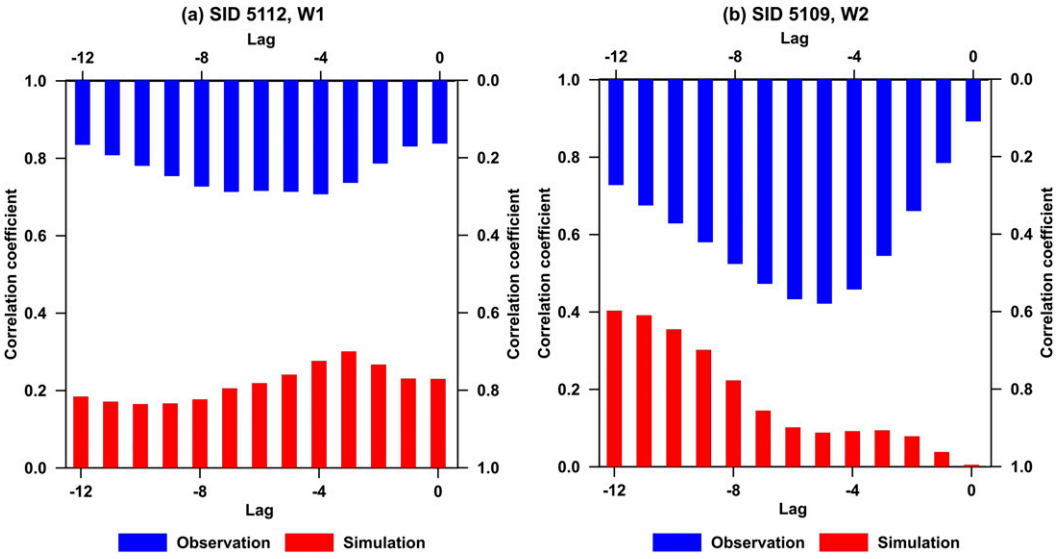

FIG. 12. The cross-correlation function plots for hourly mean areal precipitation compared with both the observed (blue) and simulated (red) streamflow at both SIDs 5112 and 5109 during the mid-February 2019 storm, where the rainfall data are obtained from AQPI radar, and the NWM-based WRF-Hydro system is used for streamflow simulation.

time delay between the two signals (e.g., rainfall and streamflow). Figure 12 explores the CCF for hourly MAP of AQPI radar QPE inputs compared with both the observed and simulated streamflow at SIDs 5112 and 5109 in the mid-February 2019 storm. As the NWM shows better skill than both Grid and Reach schemes in WRF-Hydro in the human-affected W2, the simulated streamflow used in this section are from the NWM results.

It is found that the most dominant cross correlations occur between lag hour −8 and −4 for the observed streamflow at both SIDs 5112 and 5109, and the largest correlations are positive with values of 0.29 (−4 h) for SID 5112 and 0.58 (−5 h) for SID 5109, respectively. This implies that the time margin from the above-average rainfall to the above-average runoff is about 4 h at SID 5112 and 5 h at SID 5109. Since the drainage area of W1 is smaller than that of W2, the lag response at SID 5112 is faster than that of SID 5109. In addition, there is a large difference in the CCF pattern between rainfall and simulated streamflow at SID 5109 corresponding to the rainfall and observed streamflow in W2. Specifically, there is around 12 h delay before the highest correlation value (0.40) is achieved for the simulated streamflow. The slower response for the observed streamflow at SID 5109 might come from the regulation of reservoirs in W2.

5. Concluding remarks

A WRF-Hydro experiment is performed in two different watersheds (natural and human-affected) in AR-driven rain events of February 2019 to quantify the potential of AQPI gap-filling radar network for streamflow simulation in the Bay Area. The primary findings are summarized as follows:

1) The NWM configuration can reproduce observed streamflow hydrograph in terms of volume and shape in the human-influenced watershed (i.e., W2). It also performs better than both the Grid and Reach configurations, partly because Grid/Reach fail to translate accurate water fluxes and states from the fine grids to the aggregated catchment in W2.
2) The AQPI radar rainfall product without gauge correction provides better simulated streamflow in the larger watershed containing reservoirs compared with the NEXRAD-forced simulation. This is also consistent with better performance of the AQPI gap-filling radar on the rainfall estimates compared with NEXRAD.
3) Increasing channel roughness coefficient, i.e., Mann, decreases the simulated peak flow and further lags the associated peak timing. In addition, the discharge increases to a higher level as the infiltration factor, i.e., REFKDT, decreases in the survey watershed.
4) There is a longer lag response for the observed streamflow in W2 (managed) compared to W1 (natural), which suggests that reservoirs play an important role for regulating the flow time response in the human-affected watershed.
5) Based on the simulation and sensitivity analysis, the large variability of the simulated river flows from three configurations using the same AQPI radar QPE forcing compared with the relatively small differences of simulated flows from the two radar products (AQPI and NEXRAD) suggests that the routing configuration plays a more important role than the rainfall forcing itself in affecting the hydrologic response and functional behavior of the simulations.

This study indicates that the AQPI gap-filling X-band radar network has great potential for supporting streamflow simulations in the Bay Area. This results further illustrate the link between heavy rainfall and streamflow response through the WRF-Hydro system. However, it is still challenging to

accurately simulate the streamflow hydrographs including volume and peak for these extreme rainfall events. There is currently no representation of overbank flow processes and the interaction with the hydrogrids, and the flow into the channel is one-way in the WRF-Hydro modeling system (Gochis et al. 2018). It fails to explicitly model the inundation area from overbank flow from the channel back to the terrain in these heavy rainfall events. The next step will focus on the issue of overbank flow mode designation so as to improve the performance of the WRF-Hydro application in the Bay Area rainfall events.

Acknowledgments. This study was supported by the California Department of Water Resources, the Sonoma County Water Agency, and the NOAA Physical Sciences Laboratory. The authors thank Dr. Peirong Lin from Princeton University for the helpful suggestions. We are also very grateful to the editors and the anonymous reviewers for their critical comments and thoughtful suggestions.

REFERENCES

Arnault, J., S. Wagner, T. Rummler, B. Fersch, J. Bliefernicht, S. Andresen, and H. Kunstmann, 2016: Role of runoff–infiltration partitioning and resolved overland flow on land–atmosphere feedbacks: A case study with the WRF-Hydro coupled modeling system for West Africa. *J. Hydrometeor.*, **17**, 1489–1516, https://doi.org/10.1175/JHM-D-15-0089.1.

——, and Coauthors, 2018: Precipitation sensitivity to the uncertainty of terrestrial water flow in WRF-Hydro: An ensemble analysis for central Europe. *J. Hydrometeor.*, **19**, 1007–1025, https://doi.org/10.1175/JHM-D-17-0042.1.

——, and Coauthors, 2019: A joint soil-vegetation-atmospheric water tagging procedure with WRF-Hydro: Implementation and application to the case of precipitation partitioning in the Upper Danube River Basin. *Water Resour. Res.*, **55**, 6217–6243, https://doi.org/10.1029/2019WR024780.

Berne, A., and W. F. Krajewski, 2013: Radar for hydrology: Unfulfilled promise or unrecognized potential? *Adv. Water Resour.*, **51**, 357–366, https://doi.org/10.1016/j.advwatres.2012.05.005.

Bringi, V. N., and V. Chandrasekar, 2001: *Polarimetric Doppler Weather Radar: Principles and Applications*. Cambridge University Press, 636 pp.

Chandrasekar, V., H. Chen, and B. Philips, 2018: Principles of high-resolution radar network for hazard mitigation and disaster management in an urban environment. *J. Meteor. Soc. Japan*, **96A**, 119–139, https://doi.org/10.2151/jmsj.2018-015.

Chao, L., K. Zhang, Z. Yang, J. Wang, P. Lin, J. Liang, Z. Li, and Z. Gu, 2020: Improving flood simulation capability of the WRF-Hydro-RAPID model using a multi-source precipitation merging method. *J. Hydrol.*, **592**, 125814, https://doi.org/10.1016/j.jhydrol.2020.125814.

Chen, H., R. Cifelli, and A. White, 2020: Improving operational radar rainfall estimates using profiler observations over complex terrain in northern California. *IEEE Trans. Geosci. Remote Sens.*, **58**, 1821–1832, https://doi.org/10.1109/TGRS.2019.2949214.

Cifelli, R., V. Chandrasekar, H. Chen, and L. E. Johnson, 2018: High resolution radar quantitative precipitation estimation in the San Francisco Bay Area: Rainfall monitoring for the urban environment. *J. Meteor. Soc. Japan*, **96A**, 141–155, https://doi.org/10.2151/jmsj.2018-016.

Cristiano, E., M. C. ten Veldhuis, and N. van de Giesen, 2017: Spatial and temporal variability of rainfall and their effects on hydrological response in urban areas—A review. *Hydrol. Earth Syst. Sci.*, **21**, 3859–3878, https://doi.org/10.5194/hess-21-3859-2017.

Dugger, A. L., and Coauthors, 2017: Learning from the National Water Model: Regional improvements in streamflow prediction through experimental parameter and physics updates to the WRF-Hydro Community Model. *31st Conf. on Hydrology*, Seattle, WA, Amer. Meteor. Soc., 6A.3, https://ams.confex.com/ams/97Annual/webprogram/Paper314352.html.

Ek, M. B., and Coauthors, 2003: Implementation of Noah land surface model advances in the National Centers for Environmental Prediction operational mesoscale Eta model. *J. Geophys. Res.*, **108**, 8851, https://doi.org/10.1029/2002JD003296.

Garcia, R., and R. A. Kahawita, 1986: Numerical solution of the St. Venant equations with the MacCormack finite-difference schemes. *Int. J. Numer. Methods Fluids*, **6**, 259–274, https://doi.org/10.1002/fld.1650060502.

Gochis, D. J., and Coauthors, 2018: The WRF-Hydro modeling system technical description (version 5.0). NCAR Tech. Note, 107 pp., https://ral.ucar.edu/sites/default/files/public/WRF-HydroV5TechnicalDescription.pdf.

Gupta, H. V., H. Kling, K. K. Yilmaz, and G. F. Martinez, 2009: Decomposition of the mean squared error and NSE performance criteria: Implications for improving hydrological modelling. *J. Hydrol.*, **377**, 80–91, https://doi.org/10.1016/j.jhydrol.2009.08.003.

Gustafsson, N., and Coauthors, 2018: Survey of data assimilation methods for convective-scale numerical weather prediction at operational centres. *Quart. J. Roy. Meteor. Soc.*, **144**, 1218–1256, https://doi.org/10.1002/qj.3179.

Hatchett, B., and Coauthors, 2020: Observations of an extreme atmospheric river storm with a diverse sensor network. *Earth Space Sci.*, **6**, e2020EA001129, https://doi.org/10.1029/2020EA001129.

Johnson, J. M., D. Munasinghe, D. Eyelade, and S. Cohen, 2019: An integrated evaluation of the National Water Model (NWM)–Height Above Nearest Drainage (HAND) flood mapping methodology. *Nat. Hazards Earth Syst. Sci.*, **19**, 2405–2420, https://doi.org/10.5194/nhess-19-2405-2019.

Johnson, L. E., R. C. Ifelli, and A. B. White, 2020: Benefits of an advanced quantitative precipitation information system. *J. Flood Risk Manage.*, **13**, e12573, https://doi.org/10.1111/jfr3.12573.

Jordan, R, 1991: one-dimensional temperature model for a snow cover: Technical documentation for SNTERERM.89. Special Rep. 91-16, Cold Region Research and Engineers Laboratory, U.S. Army Corps of Engineers, Hanover, NH, 61 pp.

Krajewski, W. F., and J. A. Smith, 2002: Radar hydrology: Rainfall estimation. *Adv. Water Resour.*, **25**, 1387–1394, https://doi.org/10.1016/S0309-1708(02)00062-3.

Lahmers, T. M., H. Gupta, C. L. Castro, D. J. Gochis, D. Yates, A. Dugger, D. Goodrich, and P. Hazenberg, 2019: Enhancing the structure of the WRF-Hydro hydrologic model for semiarid environments. *J. Hydrometeor.*, **20**, 691–714, https://doi.org/10.1175/JHM-D-18-0064.1.

Lin, P., Z.-L. Yang, D. J. Gochis, W. Yu, D. R. Maidment, M. A. Somos-Valenzuela, and C. H. David, 2018: Implementation of a vector-based river network routing scheme in the community WRF-Hydro modeling framework for flood discharge simulation. *Environ. Modell. Software*, **107**, 1–11, https://doi.org/10.1016/j.envsoft.2018.05.018.

Liu, Y., J. Liu, C. Li, F. Yu, W. Wang, and Q. Qiu, 2021: Parameter sensitivity analysis of the WRF-Hydro modeling system for streamflow simulation: A case study in semi-humid and semi-arid catchments of northern China. *Asia Pac. J. Atmos. Sci.*, **57**, 451–466, https://doi.org/10.1007/s13143-020-00205-2.

Ma, Y., and V. Chandrasekar, 2020: A hierarchical Bayesian approach for bias correction of NEXRAD dual-polarization rainfall estimates: Case study on Hurricane Irma in Florida. *IEEE Geosci. Remote Sens. Lett.*, **18**, 568–572, https://doi.org/10.1109/LGRS.2020.2983041.

Naabil, E., B. L. Lamptey, J. Arnault, A. Olufayo, and H. Kunstmann, 2017: Water resources management using the WRF-Hydro modelling system: Case-study of the Tono Dam in West Africa. *J. Hydrol. Reg. Stud.*, **12**, 196–209, https://doi.org/10.1016/j.ejrh.2017.05.010.

Niu, G., and Coauthors, 2011: The community Noah land surface model with multi-parameterization options (Noah-MP): 1. Model description and evaluation with local-scale measurements. *J. Geophys. Res.*, **116**, D12109, https://doi.org/10.1029/2010JD015139.

Ralph, F. M., and Coauthors, 2016: CalWater field studies designed to quantify the roles of Atmospheric Rivers and aerosols in modulating U.S. West Coast precipitation in a changing climate. *Bull. Amer. Meteor. Soc.*, **97**, 1209–1228, https://doi.org/10.1175/BAMS-D-14-00043.1.

Rummler, T., J. Arnault, D. J. Gochis, and H. Kunstmann, 2019: Role of lateral terrestrial water flow on the regional water cycle in a complex Terrain region: Investigation with a fully coupled model system. *J. Geophys. Res. Atmos.*, **124**, 507–529, https://doi.org/10.1029/2018JD029004.

Sellers, P. J., M. D. Heiser, and F. G. Hall, 1992: Relations between surface conductance and spectral vegetation indices at intermediate (100 m^2 to 15 km^2) length scales. *J. Geophys. Res.*, **97**, 19 033–19 059, https://doi.org/10.1029/92JD01096.

Senatore, A., G. Mendicino, D. J. Gochis, W. Yu, D. Yates, and H. Kunstmann, 2015: Full coupled atmosphere-hydrology simulations for the central Mediterranean: Impact of enhanced hydrological parameterization for short and long time scales. *J. Adv. Model. Earth Syst.*, **7**, 1693–1715, https://doi.org/10.1002/2015MS000510.

Seo, D. J., E. Habib, H. Andrieu, and E. Morin, 2015: Hydrologic applications of weather radar. *J. Hydrol.*, **531**, 231–233, https://doi.org/10.1016/j.jhydrol.2015.11.010.

Sharma, A., C. Wasko, and D. P. Lettenmaier, 2018: If precipitation extremes are increasing, why aren't floods? *Water Resour. Res.*, **54**, 8545–8551, https://doi.org/10.1029/2018WR023749.

Tolson, B. A., and C. A. Shoemaker, 2007: Dynamically dimensioned search algorithm for computationally efficient watershed model calibration. *Water Resour. Res.*, **43**, W01413, https://doi.org/10.1029/2005WR004723.

Viterbo, F., and Coauthors, 2020: A multiscale, hydrometeorological forecast evaluation of National Water Model forecasts of the May 2018 Ellicott City, Maryland, Flood. *J. Hydrometeor.*, **21**, 475–499, https://doi.org/10.1175/JHM-D-19-0125.1.

Wehbe, Y., and Coauthors, 2019: Analysis of an extreme weather event in a hyper-arid region using WRF-Hydro coupling, station, and satellite data. *Nat. Hazards Earth Syst. Sci.*, **19**, 1129–1149, https://doi.org/10.5194/nhess-19-1129-2019.

White, A. B., B. J. Moore, D. J. Gottas, and P. J. Neiman, 2019: Winter storm conditions leading to excessive runoff above California's Oroville dam during January and February 2017. *Bull. Amer. Meteor. Soc.*, **100**, 55–70, https://doi.org/10.1175/BAMS-D-18-0091.1.

Xia, Y., and Coauthors, 2012: Continental-scale water and energy flux analysis and validation for the North American Land Data Assimilation System project phase 2 (NLDAS-2): 1. Intercomparison and application of model product. *J. Geophys. Res.*, **117**, D03109, https://doi.org/10.1029/2011JD016048.

Yang, Z., X. Cai, G. Zhang, A. Tavakoly, Q. Jin, L. Meyer, and X. Guan, 2011: The Community Noah Land Surface Model with Multi-Parameterization Options (Noah-MP): Technical description. The University of Texas at Austin, 75 pp., https://www.jsg.utexas.edu/noah-mp/files/Noah-MP_Technote_v0.2.pdf .

Yucel, I., A. Onen, K. K. Yilmaz, and D. Gochis, 2015: Calibration and evaluation of a flood forecasting system: Utility of numerical weather prediction model, data assimilation and satellite-based rainfall. *J. Hydrol.*, **523**, 49–66, https://doi.org/10.1016/j.jhydrol.2015.01.042.

Zhang, J., and Coauthors, 2011: National Mosaic and Multi-Sensor QPE (NMQ) system: Description, results, and future plans. *Bull. Amer. Meteor. Soc.*, **92**, 1321–1338, https://doi.org/10.1175/2011BAMS-D-11-00047.1.

——, P. Lin, S. Gao, and Z. Fang, 2020: Understanding the reinfiltration process to simulating streamflow in north central Texas using the WRF-Hydro modeling system. *J. Hydrol.*, **587**, 124902, https://doi.org/10.1016/j.jhydrol.2020.124902.